https://doi.org/10.5194/egusphere-2026-137
Preprint. Discussion started: 6 February 2026

Ultra-Lightweight Mid-IR Methane Sensor for UAV-based Measurements

Meghan N. Beattie[1], Chase Sun[1], Roger MacLeod[2], Nicaulas A. Sabourin[3], Peter D. Morse[4], Greg J. Smallwood[1], Joel C. Corbin[1], and Jalal Norooz Oliaee[1]

[1]Metrology Research Centre, National Research Council Canada, 1200 Montreal Road, Ottawa, ON K1A 0R6, Canada
[2]Geological Survey of Canada, Pacific Division, Natural Resources Canada, 9860 W. Saanich Road, Sidney, British Columbia, V8L 4B2, Canada
[3]Quantum and Nanotechnologies Research Centre, National Research Council Canada, 1200 Montreal Road, Ottawa, Ontario, K1A 0R6, Canada
[4]Geological Survey of Canada, Natural Resources Canada, 601 Booth Street, Ottawa, Ontario, K1A 0E8, Canada

Correspondence: Jalal Norooz Oliaee (Jalal.NoroozOliaee@nrc-cnrc.gc.ca)

Abstract. We developed an ultra-lightweight mid-infrared laser spectroscopic sensor for precise, rapid mobile measurements of atmospheric methane concentrations aboard small uncrewed aerial vehicles. The design is simple and compact, featuring a Herriott-type multi-pass cell in an open-path configuration. A single board computer with two on-chip microprocessor units allows rapid data acquisition and onboard wavelength modulation spectroscopy, making the sensor a stand-alone turnkey instrument. Including the dedicated battery, the sensor weighs 1.2 kg and consumes up to 11 W of electrical power under standard laboratory conditions making it one of the most lightweight sensors reported. The measurement resolution is 3.7 ppb at a 1 s averaging time. We deployed the sensor in controlled-release experiments and detected methane flux rates as low as 0.2 $\mathrm{kg\,h^{-1}}$. Consequently, it can be deployed to measure fugitive emissions from anthropogenic and natural sources that would be undetectable for other methods.

1 Introduction

Methane emissions to the atmosphere, from both anthropogenic and natural processes, typically originate at or near the Earth's surface. Until recently, technologies for in-situ measurement surveys of surface-based emissions were primarily limited to ground-level approaches via motor vehicles (Caulton et al., 2018), bicycles (MacKay et al., 2021; Vogel et al., 2024), ships (Berchet et al., 2020), or on foot (Maazallahi et al., 2023), as well as airborne surveys using crewed aircraft (Han et al., 2024; Khaleghi et al., 2024; Tyner and Johnson, 2021).

Vehicle-based mobile surveys are generally restricted to the route of travel (e.g. roadways, pathways, water channels, etc.) and provide information about a gaseous plume only at a single height, typically < 3 m above the ground. Meanwhile, emission plumes often extend well above the measurement platform, necessitating the use of plume models, including the well-known

https://doi.org/10.5194/egusphere-2026-137
Preprint. Discussion started: 6 February 2026

Gaussian plume model, that depend on numerous simplifying assumptions to estimate emission fluxes (Blackmore et al., 2024; Kumar et al., 2022, 2021; Zhou et al., 2019; Caulton et al., 2018). In practice, complex terrain effects, recirculation zones, and vertical wind shear can produce inhomogeneous wind fields and less predictable plume behavior (Fish et al., 2025; Wharton et al., 2023), which often lead to substantial uncertainties when calculating emission fluxes.

Conversely, crewed aircraft have minimum safe flight altitudes that are typically > 100 m above ground level. As such, they generally do not capture the full vertical extent of a plume, requiring extrapolation over hundreds of meters between the lowest flight altitude and the ground. This extrapolation requires assumptions about plume behavior and local meteorological conditions, potentially resulting in inaccuracies when deriving plume emission rates (Gordon et al., 2015). Consequently, crewed aircraft measurements must be performed at much greater distances from the emission source than is required for ground-based measurements. Dispersion and dilution over these distances results in lower methane concentrations in the plume and a lower probability of detection. For this reason, extremely stable and sensitive instruments are required for aircraft-based surveys.

Unlike crewed aircraft, uncrewed aerial vehicles (UAVs), also known as remotely piloted aircraft systems (RPAS) or drones, may operate with minimum flight altitudes as low as 1 m above the ground. UAVs offer a maneuverable and flexible platform that fills in the measurement gap between ground-based and crewed aircraft surveys. UAVs also provide the capability to acquire near-surface measurements in regions that are difficult or dangerous to access by ground-based platforms, such as wetlands, permafrost terrains, or geologically unstable areas, as well as industrial or contaminated environments where human exposure would pose risks to health and safety. In the past two decades, a combination of technological advances and new policies and regulations have contributed to the widespread availability and practical use of small (< 25 kg) consumer- and enterprise-grade UAVs. However, the limited availability of compact, lightweight, and high-precision gas sensors suitable for UAV deployment has, until recently, impeded the widespread adoption of UAV technology for surveying methane emissions.

Advances in methane sensing technologies are contributing to a new generation of compact methane sensors, and several spectroscopic measurement methods with different implementations have been reported for UAV-based detection of methane (Golston et al., 2017; Shaw et al., 2021; Thorpe et al., 2017; Tuzson et al., 2020). They generally fall into two measurement categories: in-situ and ex-situ. For in-situ measurements–also called point measurements–the geo-tagged gas concentration is measured at the location of the sensor. In contrast, for ex-situ measurements–also referred to as remote sensing, imaging spectroscopy, or gas imaging and mapping–the column-integrated gas concentration is usually inferred from surface-scattered light signals detected at the position of the aerial platform; though ex-situ aerial measurements can also be conducted using ground-based instrumentation coupled with a UAV-mounted retro-reflector (Cossel et al., 2017). Remote sensing techniques generally provide broader spatial coverage and can often map emission plumes more quickly than point measurements, making them well suited for large-scale surveys and the rapid localization and quantification of emission “hot spots.” However, their detection limit is often dependent on the flight altitude and the properties of the scattering surface. In-situ instruments, which measure gas concentrations within an onboard sampling cell, are able to detect much smaller concentration enhancements. These point sensors take longer than an ex-situ instrument to sample the same area, but are well-suited to ground truthing, to targeted local deployments for the detection of small methane enhancements, and to deployments over surfaces that are challenging or unsuitable for instruments that rely on surface-scattered light, such as water or wetlands.

Among in-situ gas analyzers, closed-path and open-path sampling systems have been developed (Detto et al., 2011). Closed-path configurations use a sampling pump to move ambient air through an enclosed sampling cell. The sampling cell is protected from the environment, but exchange rates and mixing within the cell cause a delayed response and affect the recorded plume shape (Takriti et al., 2021). When concentration values are geo-tagged, these effects can introduce a large error that must be accounted for, adding additional effort during data processing. In contrast, open-path instruments measure ambient air directly, offering near-instantaneous response times. With no sampling pumps, they are lighter and consume less power than closed-cell instruments. However, optical elements exposed to the environment require more frequent maintenance (i.e. cleaning). This maintenance requirement that adds to the complexity and challenge of long-unattended deployments of open-path systems (McDermitt et al., 2011), but does not cause operational limitations for deploying on UAVs with short flight times.

In this paper, we present an ultra-lightweight open-path laser spectroscopic methane sensor that we developed for deployment on small UAVs. Similar to an earlier prototype (Norooz Oliaee et al., 2022), the present system employs a 3270 nm GaSb-based distributed feedback (DFB) tunable diode laser that targets the strong ν_3 mid-infrared (mid-IR) methane absorption band, enabling high-precision measurements. The novelty of the current sensor platform lies in its unique combination of high performance with lightweight, compact design, which could facilitate the widespread adoption and deployment of such rapid-response laser-based gas sensors on small UAVs or other suitable platforms. The sensor features a compact open-path Herriot-type absorption cell and a low-cost single-board computer (SBC) performs real-time signal generation, acquisition, and data processing for wavelength-modulation spectroscopy (WMS). Although our research demonstrates the sensor's application for methane, the same platform could be adapted to other gaseous species by substituting the laser and photodetector to target absorption features specific to the molecule of interest. Differences in atmospheric abundance or absorption cross section may require further optomechanical or electronics adaptations; however, the core design principles remain broadly transferable.

Here we report the sensor architecture, including the compact and simple optical assembly, integrated electronics, single-board computer (SBC), and custom data acquisition board that have been instrumental in achieving a lightweight, power-efficient, and high-precision sensor with onboard data processing. We present the instrument's laboratory and field performance along with results from controlled-release experiments that demonstrate its potential for methane leak detection and emission rate quantification when deployed on a small enterprise-grade UAV.

2 Methods

2.1 Measurement principle

The sensor is based on mid-IR tunable diode laser absorption spectroscopy (TDLAS). In this method, the wavelength of a mid-IR diode laser is tuned across an absorption line in the fundamental ν_3 absorption band of methane. Unlike direct absorption spectroscopy (DAS), in which the gas concentration is determined directly from the transmission spectrum, we employ WMS, in which the laser wavelength is swept across the molecular absorption line and modulated sinusoidally. Detection of the filtered and demodulated signal at harmonics of the modulation frequency enhances the signal-to-noise ratio and the measurement sensitivity. The gas concentration is retrieved from the amplitude of the corresponding peak in the second harmonic spectrum.

2.2 Optical assembly

Fig. 1(a) shows representative schematic of the sensor's optical head. We use a collimated free-space GaSb-based DFB diode laser (NL3270-TL, Norcada, Canada) tuned to a central wavelength of 3270.4 nm at a laser temperature of around 7 °C with an injection current of 130 mA. The laser light is launched into an open-path multi-pass Herriott cell, chosen for its simplicity and compatibility with commercial off-the-shelf mirrors. We used a custom ray-tracing script, based on analytical solutions of the optical cavity geometry without invoking the paraxial approximation, to guide the optomechanical design, similar to (Cui et al., 2019; Engel and Moyer, 2007). The cell is composed of two 25.4 mm-diameter gold-coated concave spherical mirrors (CM254-100EH3-M02, Thorlabs, USA) with focal lengths of 100.0 mm and an off-axis hole 7.0 mm from the center of each mirror for passing the laser beam. The on-axis mirror separation distance in the cell is 131.4 mm. The laser beam is oriented to produce precessing circular patterns on the two mirrors, resulting in 35 passes and an effective path length of 4.600 m, as shown in Fig. 1(a).

The laser beam exiting the multi-pass cell is directed and focused onto an optically-immersed HgCdTe photovoltaic detector (PVI-2TE-4-1x1-TO8-wAl2O3-36, Vigo Photonics, Poland) using an off-axis parabolic mirror (MPD01M9-M01, Thorlabs, USA).

2.3 Mechanical assembly

The laser, its heatsink, both mirrors of the multi-pass cell, and the off-axis parabolic mirror are integrated into a rigid, cage-like assembly that reduces the effects of mechanical vibrations during UAV flight deployments (see Fig. 1(c)). The optomechanical design has no moving parts and the optical alignment is performed during the assembly procedure, using shims to achieve the correct laser injection angle. The optical assembly, photodetector, and electronic components are affixed to an aluminum base-plate. The sensor package is compact and easily portable, with outer dimensions of 23.5 cm (L) × 12.5 cm (W) × 9.5 cm (H). Including all electronics, batteries, and peripheral devices such as ambient condition sensors and a GPS receiver, the mass of the sensor package is just 1.2 kg. This is well within the payload limits of many small consumer- or enterprise-grade UAVs such as the DJI Matrice 300 RTK used in this study, as described in Section 2.6.

2.4 Temperature control and power consumption

Both the laser and the photodetector are temperature-stabilized via integrated thermoelectric coolers (TECs), controlled by ultra-stable TEC controllers (WTC32ND, Wavelength Electronics, USA) mounted on custom-designed printed circuit boards (PCBs). The PCBs were adapted from the manufacturer's evaluation board (WTC32ND-EV, Wavelength Electronics, USA) with added fail-safe protection circuitry to prevent accidental thermal runaway events. The laser temperature is regulated to an average of 7.4 °C, while the detector is cooled to -42.7 °C.

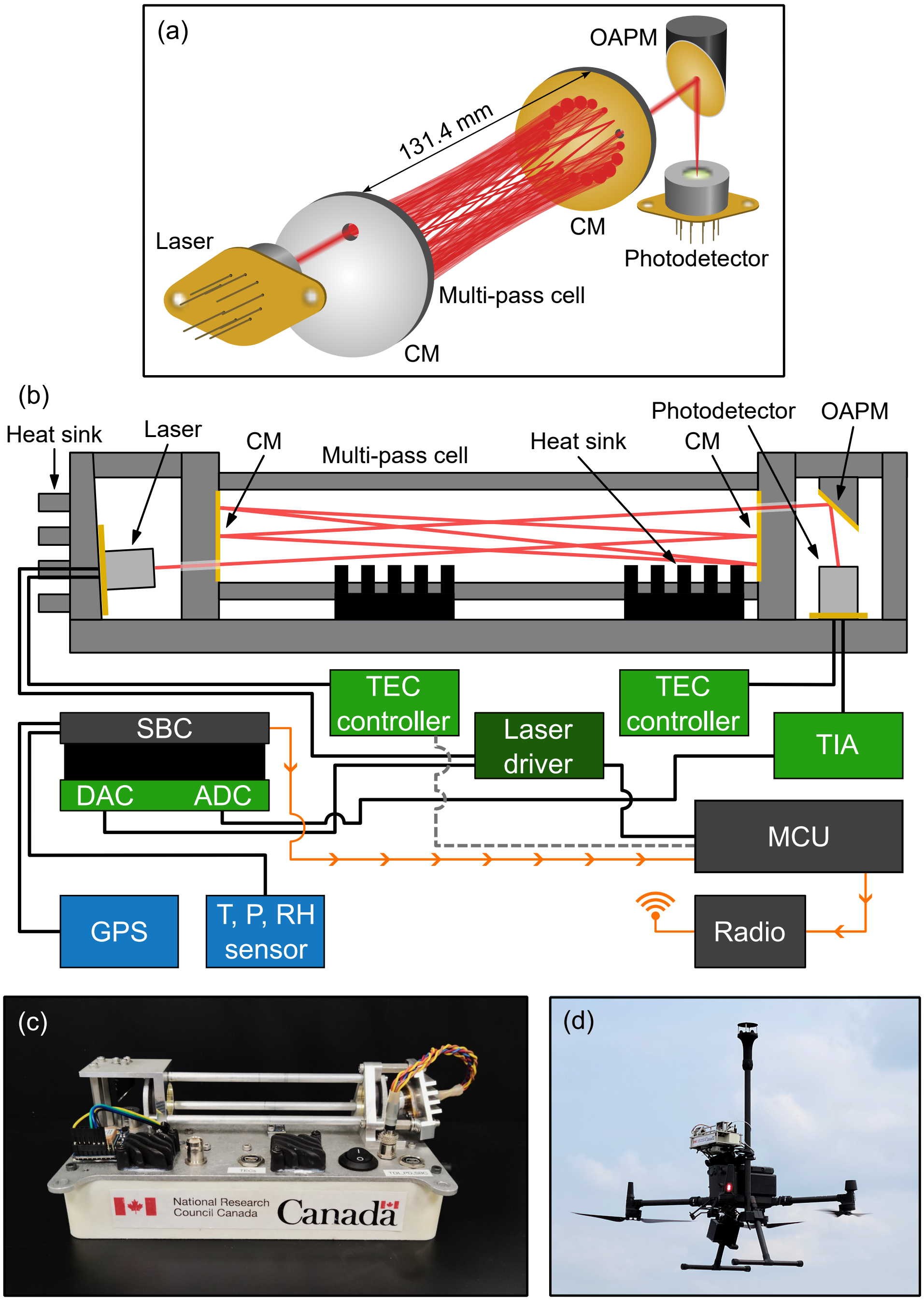

Figure 1. (a) Schematic of methane sensor optical head showing laser beam trajectory. (b) Schematic showing sensor components and electrical connections. For clarity, power supply is not shown. CM: concave mirror; OAPM: off-axis parabolic mirror; SBC: single board computer; TEC: thermoelectric cooler; TIA: transimpedance amplifier; MCU: microcontroller unit. (c) Close up of ultra-lightweight methane sensor. (d) Sensor and Gill WindUltra anemometer deployed on a DJI Matrice 300 RTK UAV.

https://doi.org/10.5194/egusphere-2026-137
Preprint. Discussion started: 6 February 2026

The sensor is powered by a 5 VDC supply delivered through two mini type-B USB ports, which can be conveniently driven by a standard power pack with dual type-A USB outputs that each provide a minimum 2 A current output to sustain the TEC operation on startup. At room temperatures and in steady-state, the sensor package (including the SBC) consumes around 11 W of electrical power. More than half of the power draw is attributed to the two TECs and their controllers, with the photodetector TEC being the dominant consumer. At colder air temperatures, the overall power consumption decreases due to the reduced load on the photodetector TEC.

2.5 Onboard signal generation, acquisition, and processing

A schematic of the electrical interconnections is shown in Fig. 1(b). Signal generation and processing is handled onboard and in real time by a BeagleBone Black SBC (BeagleBoard.org, USA). The SBC is furnished with a custom PCB that houses a 12-bit digital-to-analog converter (DAC; AD5621, Analog Devices, USA) and a 16-bit analog-to-digital converter (ADC; MCP33131D-10, Microchip, USA). The DAC and ADC are interfaced with the SBC via two 32-bit 200 MHz on-chip programmable real-time units (PRUs) and a memory buffer, which enables data transfer rates to be independent of the Linux operating system processes. The PRUs have a timing accuracy of 5 ns, which is suitable for the fast data generation and acquisition typically required in kHz-range WMS applications.

The DAC translates digital modulation patterns computed numerically by the SBC to analog voltages at a sampling rate of 400 kHz. This analog signal is fed to a low noise laser diode driver (DRV200-A-200, Koheron, France) as modulation input. The driver simultaneously provides a constant DC offset current, enabling the central laser wavelength to be tuned to the methane absorption line at 3270.4 nm. The laser injection current is swept from 110 mA to 200 mA in a sawtooth pattern with a frequency of 100 Hz, producing a corresponding wavelength sweep rate of approximately 20 $\mathrm{pm\ mA^{-1}}$ near the target wavelength. A sinusoidal modulation with a frequency of 10 kHz and a peak amplitude of 15 mA is added to the current ramp for the purpose of noise rejection by wavelength modulation (Fig. 2).

The photocurrent signal from the photodetector is converted to a voltage using a custom transimpedance amplifier (TIA). The analog voltage signal from the TIA is acquired by the ADC at a sampling rate of 312.5 kHz. The SBC computes the second harmonic $(2f)$ spectrum, $X_{2f}(t)$, from the raw time-dependent detector signal, $I_t(t)$, by applying a digital lock-in amplifier:

$$X_{2f}(t) = LP\{I_t(t) \times \cos(2\pi t \cdot 2f + \phi)\} \tag{1}$$

where t is time, f is the modulation frequency, ϕ is the detection phase, and LP is a digital low-pass filter. For the latter, a numerical cascaded second order biquad filter with a cut-off frequency of 700 Hz is applied. The detection phase is selected empirically to maximize the magnitude of the methane peak in the second harmonic spectrum. The amplitude of the methane peak is computed using a simple search algorithm to find the methane peak and left-side trough in the $2f$ spectrum by looking for the minimum and maximum values within predefined bounds. The peak-to-peak amplitude is used to compute the methane concentration by calibrating to reference gas concentrations, as described in section 3.1.

The SBC records the computed methane concentration as a function of time at a rate of 100 Hz along with ambient temperature, pressure, and humidity data, which are measured by an onboard sensor (BME280, Bosch Sensortec, Germany). A GPS

https://doi.org/10.5194/egusphere-2026-137
Preprint. Discussion started: 6 February 2026

module (Ultimate GPS, Adafruit, USA) is used to timestamp the data relative to coordinated universal time (UTC). The SBC saves all timestamped data to a microSD card. Optionally, raw data files containing the detector signal and the $2f$ spectrum can also be saved.

In addition to the data saved locally at 100 Hz, a down-sampled and averaged data stream with a rate of 5 Hz is passed over a universal asynchronous receiver-transmitter (UART) connection to a microcontroller unit (MCU; Metro Mini, Adafruit Industries, USA), which acts as a data hub. The MCU board also monitors the laser temperature, acting as a digital interlock that shuts off the laser driver if the laser temperature is not within pre-defined bounds. The MCU optionally feeds the down-sampled methane concentration, laser temperature, and ambient conditions data into a high-powered radio modem (RFD900x, RF Design, Australia), enabling long-distance real-time monitoring of the data stream while the sensor is deployed on a UAV. Although the data transmitted over the wireless link is not used for processing or analysis, real-time monitoring of concentration data is invaluable for guiding flight missions in the field and also for system health monitoring.

2.6 UAV integration

We deploy the 1.2 kg sensor system on a DJI Matrice 300 RTK UAV (DJI, China) that has a mass of 6.3 kg (including batteries) and a maximum payload of 2.7 kg, as shown in Fig. 1(d). The instrument is secured to the top of the UAV using a modified DJI upward gimbal connector, providing vibration isolation. We power the sensor from a 10,000 mAh power bank (Adafruit, USA), which allows the sensor to run for much longer (upwards of 2 hours) than the flight time of the UAV, and therefore does not limit the planned mission duration.

A 2D anemometer (WindUltra, Gill Instruments, UK) is also affixed to the UAV, enabling simultaneous measurement of methane concentration and wind information. The anemometer is mounted on a carbon fiber mast approximately 37 cm above the sensor's optical head and 75 cm above the UAV rotors, reducing the effect of rotor wash on the recorded wind measurements. Custom 3D-printed components secure the mast and a data logger for the anemometer to the UAV landing gear. The entire anemometer assembly including the anemometer head, mast, data logger, and battery add an additional 1.2 kg to the payload. Together, the methane sensor and anemometer systems make up a total UAV payload of 2.4 kg. The requirement for an onboard anemometer is determined by the mission goals and data analysis methods. For emission flux quantification missions, onboard wind data is highly beneficial. Conversely, for hot spot and leak detection applications, an onboard anemometer may be unnecessary if the general wind direction is known from local weather stations or models.

The true wind speed and direction $(\mathbf{u})$ are recovered from those measured by the onboard anemometer $(\mathbf{u}_{\text{anem}})$ by vector subtraction: $\mathbf{u} = \mathbf{u}_{\text{anem}} - \mathbf{v}_{\text{gnd}}$ where $\mathbf{v}_{\text{gnd}}$ is the horizontal ground velocity of the UAV. The anemometer is mounted with the "north" direction pointing to the front of the UAV and the front of the aircraft is always oriented in the direction of flight, such that onboard wind is recorded relative to the direction of travel.

Flight mission trajectories are pre-programmed and transferred to the flight controller before starting each mission to achieve systematic flight patterns. During flight, the UAV travels at a constant speed in the range of 5 to 8 $\mathrm{m\,s^{-1}}$ along each horizontal transect and cames to a stop before changing altitude or direction. With the entire payload, including the sensor and anemometer components, we achieve flight durations exceeding 20 minutes.

https://doi.org/10.5194/egusphere-2026-137
Preprint. Discussion started: 6 February 2026

2.7 Emission flux quantification

To quantify methane emission flux, we apply a direct flux quantification method that relies on the principle of mass balance (Scheutz et al., 2025; Dooley et al., 2024; Bonne et al., 2024). In this method, the UAV flies a pattern known as a "flux curtain" downwind of the methane source, consisting of stacked horizontal transects that form a vertical plane. The lateral extent of the flux curtain is chosen to ensure that the UAV traverses the entire width of the plume in each transect. The curtain height is also dictated by the size of the plume, such that elevated methane concentrations are not observed in the upper two to three transects. The vertical spacing between successive transects is minimized to give the best possible vertical resolution within the constraints of limited flight duration. The result is a two-dimensional map of the methane plume over a vertical plane downwind of the source.

Methane concentrations $[\mathrm{CH_4}]_{\mathrm{meas}}$ are recorded by the sensor at a rate of 100 Hz throughout the flight. In post-processing, a 0.1 s moving average is applied and the data is down-sampled to match the 10 Hz positional data stream from the UAV flight logs. The wind speed and direction are also recorded at a rate of 10 Hz. For each measurement point in the y-z flux curtain, the methane flux density is given by:

$$q(y,z) = \Big([\mathrm{CH_4}]_{\mathrm{meas}}(y,z) - [\mathrm{CH_4}]_{\mathrm{bkg}}(y,z)\Big) \cdot u_x(y,z) \cdot \rho_{\mathrm{CH_4}}(z) \tag{2}$$

where $[\mathrm{CH_4}]_{\mathrm{bkg}}$ is the background methane concentration, u_x is the wind speed component orthogonal to the y-z flux curtain, and $\rho_{\mathrm{CH_4}}(z)$ is the density of methane gas at altitude z. Methane density is given by $\rho_{\mathrm{CH_4}}(z) = P(z)M_{\mathrm{CH_4}}/RT$, where $M_{\mathrm{CH_4}} = 16.04$ g/mol is the molar mass of methane, R is the gas constant, and T is the average temperature. $P(z)$ denotes the pressure at altitude z, estimated by applying a linear fit to the data recorded by the onboard pressure sensor throughout the flight.

For each horizontal transect, a transect-integrated flux density $\int_{\mathrm{tr.}} q\, dy$ is calculated using the trapezoid rule for numerical integration. The total flux Q is determined by integrating over the transect-integrated flux density in the vertical direction from ground level ($z = 0$) to the top of the flux curtain.

$$Q = \int_0^{z_{\max}} \int_{\mathrm{tr.}} q(y,z)\, dy\, dz \tag{3}$$

where $z_{\max}$ is the altitude of the highest transect in the flux curtain, which should ideally exceed the vertical extent of the emission plume such that the transect-integrated flux density of the uppermost transect is zero. As such, no extrapolation is required above the flux curtain. On the other hand, plume dynamics and operational constraints often lead to non-zero flux densities in the lowest measured transect, necessitating extrapolation from the lowest transect to the ground. In this work, we define ‘virtual’ transects below the measured flux curtain and predict corresponding transect-integrated flux densities using a logarithmic wind model to generate extrapolated wind speeds and assuming a constant transect-integrated methane concentration $\int_{\mathrm{tr.}} [\mathrm{CH_4}]\, dy$ from the lowest transect to the ground. We assigned a relatively large uncertainty bound to the quantity $\int_{\mathrm{tr.}} [\mathrm{CH_4}]\, dy$ for the virtual transects, following a normal distribution for which the probability of $\int_{\mathrm{tr.}} [\mathrm{CH_4}]\, dy = 0$ is 1%. The logarithmic wind model is given by

$$u(z) = \frac{u^*}{\kappa}\ln\left(\frac{z}{z_0}\right) \tag{4}$$

where u^* is the friction velocity, z_0 is the surface roughness, and $\kappa = 0.4$ (Visscher, 2014; Bolek et al., 2024). The model is fit to altitude-dependent wind data recorded from the UAV. The corresponding 1σ prediction interval is included in the uncertainty estimates for the transect-integrated flux density for the virtual transects. Following the trapezoid rule, linear interpolation is used when integrating between transects–both measured and virtual–in Eq. 3. Uncertainties in methane concentration, wind speed, and methane density are propagated when evaluating the uncertainty on total flux Q.

3 Results and discussion

3.1 Sensor calibration and performance

The laser injection current over time is shown in Fig. 2(a) and the resultant detector signal is shown in Fig. 2(b), for ambient air with a methane concentration near 2 ppmv. The corresponding second harmonic spectrum is shown in Fig. 2(c). The 3270.4 nm absorption feature for methane is indicated, along with a nearby water absorption line centered at 3271.0 nm. At the time of measurement, the ambient temperature was 22.6°C and the relative humidity was 51.5%, yielding a water vapor concentration of approximately 1.4% v/v. The feature contained within the shaded region of Fig. 2(c) is produced by the response of the filtering function to the abrupt change in the photodetector signal from the previous laser sweep and is not indicative of light absorption.

We calibrated the sensor in an enclosed chamber with a volume of approximately 50 L under controlled gas flow conditions with a known concentration. We maintained the temperature of the gas at 21 °C by passing it through a heat exchanger with a temperature controlled thermal bath. The temperature within the enclosure was also maintained at 21 °C. Certified premixed methane-in-air gas cylinders (AirLiquide, Canada), traceable to NIST standards, were employed to achieve methane concentrations of 2.00 ppm, 5.00 ppm, 10.01 ppm, and 49.87 ppm, with associated uncertainties of $\pm 1\%$. The calibration gas flow was maintained at 15 $\mathrm{L\,min^{-1}}$ per minute using an in-line mass flow controller (MFC). We produced two additional concentrations by diluting the 49.87 ppm methane mixture with pure nitrogen, using in-line MFCs to control the mixing ratio. The mixture concentrations were quantified using a commercial methane sensor (MIRA Pico series natural gas analyzer, Aeris Technologies, USA)–recorded concentrations were 26.61 ± 0.45 ppm and 36.83 ± 0.80 ppm. Uncertainties for the in-line mixtures were estimated by comparing the methane concentrations reported by the Aeris Pico sensor to the NIST-traceable concentrations from the calibration cylinders.

For each gas concentration, the flow was established and the gas concentration was allowed to stabilize before progressing to the next concentration step. The peak-to-peak amplitude of the methane feature in the WMS $2f$ spectrum is used for concentration calibration. The response of the sensor as a function of calibration gas concentration is shown in Fig. 3. The circular markers indicate data points obtained using the calibration cylinders, whereas the diamond-shaped markers indicate the in-line gas mixtures. The response of the sensor to increasing methane concentration is nearly linear up to 10 ppm; however,

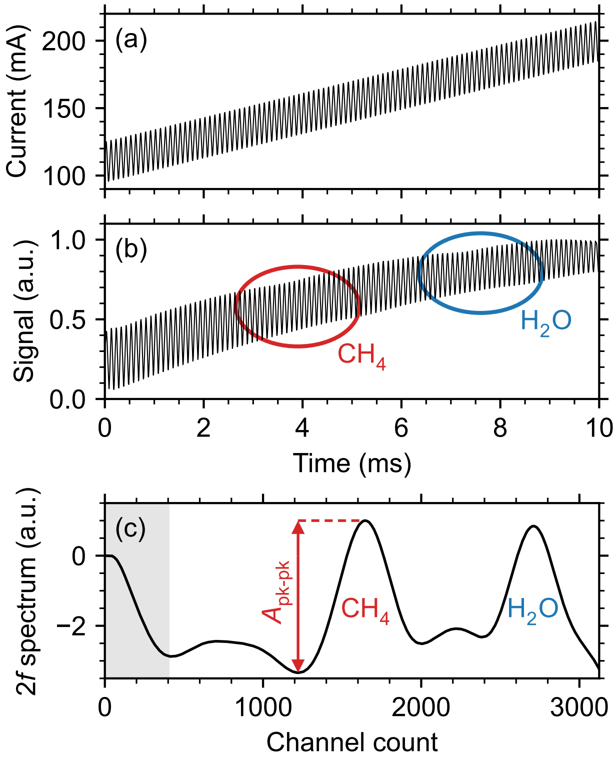

Figure 2. (a) Laser injection current ramp and 10 kHz modulation over one sawtooth period. (b) Corresponding detector signal observed under ambient measurement conditions. (c) Demodulated second harmonic spectrum. Absorption features due to CH_4 and H_2O are indicated in (b, c). The shaded region in (c) contains the initial response of the low pass filter and does not indicate absorption.

further increase in the calibration gas concentration can be described by a higher order polynomial, as previously reported in (Norooz Oliaee et al., 2022). Here, the non-linear calibration curve corresponds to a second order polynomial such that

$$[\mathrm{CH_4}](A_{\mathrm{pk-pk}}) = a \cdot A_{\mathrm{pk-pk}}^2 + b \cdot A_{\mathrm{pk-pk}} + c \qquad (5)$$

where $A_{\mathrm{pk-pk}}$ is the WMS $2f$ peak-to-peak amplitude and a, b, and c are fitting parameters. The fit parameters are obtained by orthogonal distance regression. The resultant calibration parameters for the curve shown in Fig. 3 are $a = 109 \pm 15$ ppm, $b = 98.9 \pm 3.8$ ppm, $c = -0.42 \pm 0.11$ ppm, where the uncertainties are reported to one standard deviation.

We performed a measurement of the Allan-Werle variance in the calibration enclosure for a duration of 2 hours using the 2.00 ppm methane-in-air calibration gas to determine the stability and resolution of the sensor (Fig. 4). For comparison, we generated a second Allan-Werle deviation plot using in-flight data from a period when the sensor was measuring background methane concentrations during a controlled-release experiment. The in-flight dataset only extends up to an integration time of approximately 300 s due to the limited flight duration.

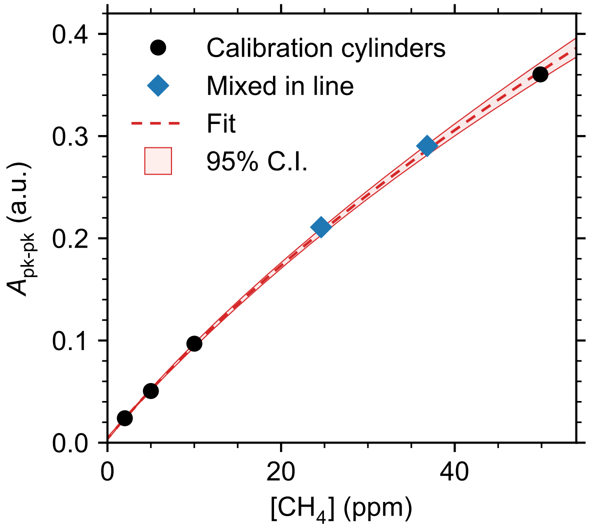

Figure 3. WMS $2f$ peak-to-peak amplitude as a function of methane concentration in the calibration gas. Fit to Eq. 5 and 95% confidence interval is shown.

Additional noise observed in-flight is primarily caused by inductive noise from the high-powered radio module used for real-time monitoring of concentration and telemetry data during flight. Though not required in all scenarios, real-time monitoring is frequently used to enable on-the-fly modification of the mission plan based on the observed methane concentrations. It may be possible to reduce this noise component by implementing design modifications such as a Faraday cage to mitigate electromagnetic interferences.

The Allan-Werle plot demonstrates that, by averaging the sensor's in-flight and laboratory concentration data up to 5.8 s and 75.9 s, respectively, corresponding optimum resolutions of 3.4 ppb and 0.8 ppb are achieved. However, for an open-path system on a mobile platform moving at 5 to 8 $\mathrm{m\,s^{-1}}$, longer averaging times (> 1 s) can result in smearing and loss of information. The averaging time that we use in this study is 0.1 s, corresponding to an in-flight resolution of 26 ppb (approximately 1.3% of current ambient methane concentrations).

The flat region in the laboratory Allan-Werle measurements below 0.1 s averaging time is attributed to hardware and software low-pass filtering of the signals, as discussed in (Werle, 2011). Fluctuations that are faster than the filter cut-off are suppressed, resulting in limited or flattened noise, which appears as random-walk or correlated noise in the Allan-Werle plot.

3.2 Controlled-release experiments

We deployed the ultra-lightweight methane sensor on the DJI Matrice 300 RTK UAV during controlled-release experiments to evaluate the sensor's capacity to detect methane emissions in the field. To simulate a methane leak, we released a small amount of methane from a methane gas cylinder (99.5% purity, AirLiquide, Canada) at a pre-determined flow rate regulated by

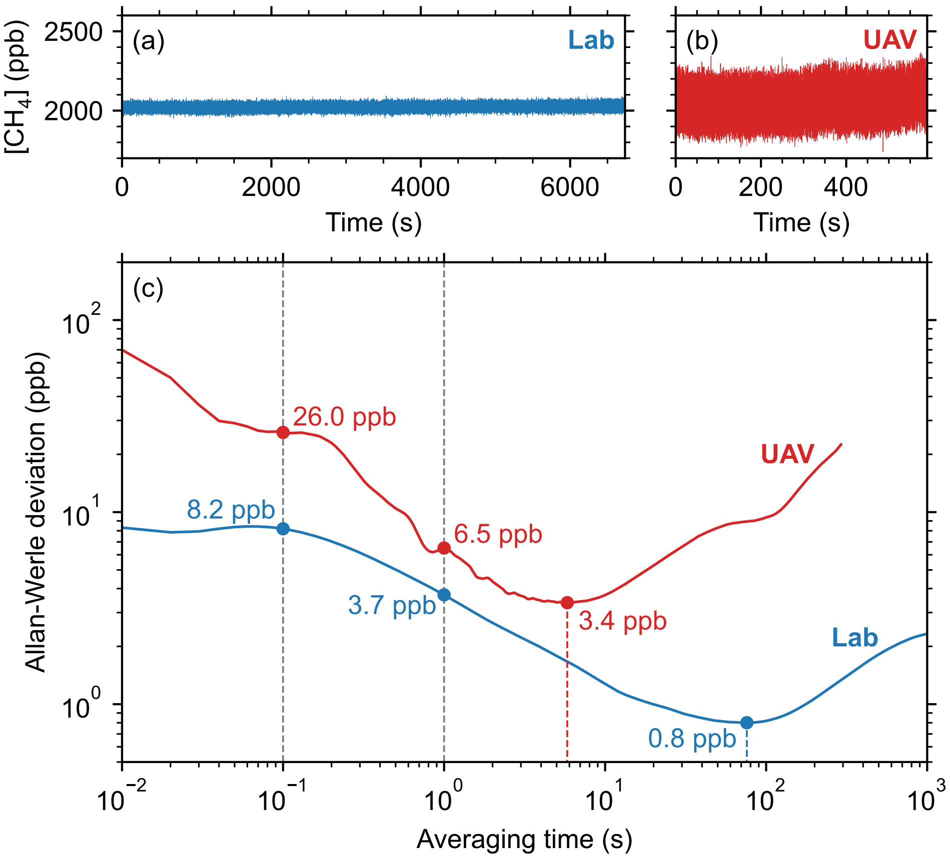

Figure 4. (a), (b) Ambient methane concentration timeseries (a) in laboratory enclosure and (b) during UAV flight. (c) Overlapping Allan-Werle deviation plots generated from the laboratory and in-flight timeseries.

an MFC. The MFC-regulated methane flow was released through a gas diffuser at the top of a mast. A stationary anemometer was positioned adjacent to the release point to record the wind speed and direction at the source location throughout each experiment. Heat maps showing the methane concentration along the UAV flight paths for two such experiments are shown in Fig. 5.

In controlled-release A, shown in Fig. 5(a), the methane flow rate was 12 standard liters per minute (SLPM; 20 °C and 101325 Pa) or 0.48 $\mathrm{kg\ h^{-1}}$ and the release point was 4.2 m above the ground. To account for adiabatic cooling of the gas upon decompression, we first passed it through a heat exchanger submersed in a thermal bath with an average temperature of 17.5 °C to achieve thermal equilibrium with the ambient temperature. We performed the experiment in a relatively open field on a day when the mean wind speed was 5.3 $\mathrm{m\ s^{-1}}$ at the release point. The UAV flew two vertical flux curtains at downwind distances of 76 m (near curtain) and 119 m (far curtain) from the emission point. Each horizontal transect spanned a lateral distance of ~240 m. Transect elevations for the near curtain, which was flown along a dirt road, ranged from 2.5 m to 19.5 m above

https://doi.org/10.5194/egusphere-2026-137
Preprint. Discussion started: 6 February 2026

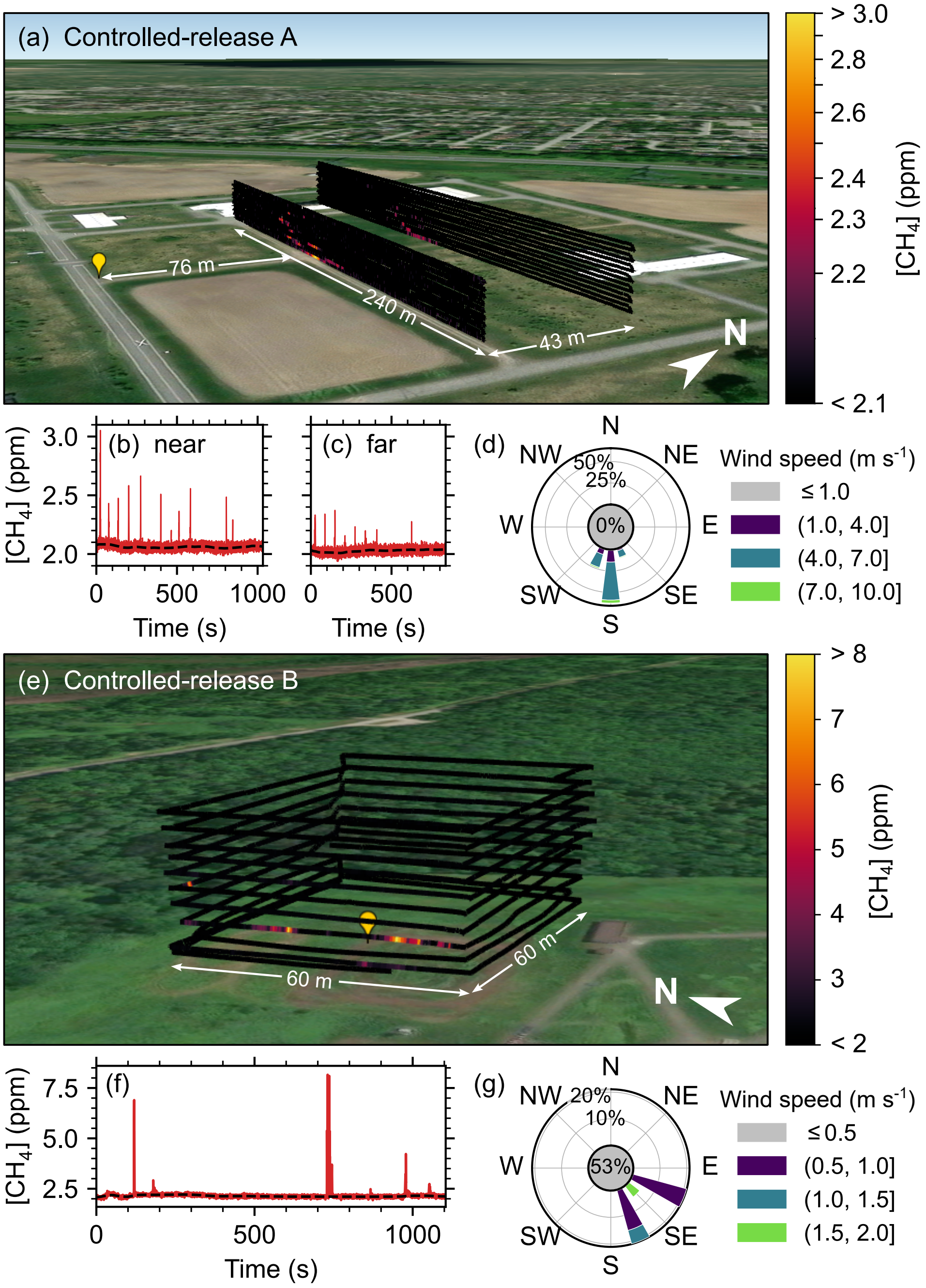

Figure 5. (a, e) Heat maps showing methane concentration along the UAV flight path for controlled-release experiments A and B. The yellow markers indicate the release points. (b, c, f) Timeseries datasets corresponding to controlled-release A (near and far curtains) and controlled-release B. The dashed black line indicates the background methane concentration. (d, g) Prevailing wind direction and speed measured at the methane release point for controlled-release A and B. (Maps Data: Google Earth, Landsat / Copernicus, ©2025 Airbus, ©2025 Maxar Technologies).

https://doi.org/10.5194/egusphere-2026-137
Preprint. Discussion started: 6 February 2026

takeoff with transect spacing of 1 m. For the far curtain, uneven terrain and vegetation near the ground prevented the UAV from flying transects below 6.5 m. Transects for the far curtain were spaced at 1.5 m intervals up to a maximum altitude of 26 m above takeoff. The average value of the background methane concentration was 2.05 ± 0.13 ppm. Elevated concentrations were detected in the middle of both flux curtains, with the highest values (near: 3.05 ± 0.18 ppm, and far: 2.37 ± 0.14 ppm) observed in the lowest transect. The corresponding timeseries data from the methane sensor is shown in Fig. 5(b, c). The flight durations were 17 minutes and 14 minutes for the near and far curtains, respectively. The prevailing wind speed and direction at the methane release point is shown in Fig. 5(d), recorded using a sonic anemometer (WindUltra, Gill Instruments, UK) at a data rate of 2 Hz.

Controlled-release B, shown in Fig. 5(e), took place in a smaller field bounded on two sides by forest. The wind was low (0.7 m s^{-1}) and highly variable in speed and direction. Methane was released from a height of 6 m at a flow rate of 5 SLPM, or 0.20 kg h^{-1}. Due to the limited space and the variable wind conditions, we executed a stacked-box UAV flight pattern consisting of stacked horizontal squares around the emission point with side lengths of 60 m. Automated box transects were flown at 3 m intervals from 4.5 m to 28.5 m above the ground. Additional transects were flown manually at elevations of 1.5 and 2.5 m when the automated flight was completed. Elevated concentrations were recorded on the box faces to the north and west, with the highest value (~8.2 ppm, compared to ~2.1 ppm background) observed in the transect at 7.5 m from the ground (see timeseries in Fig. 5(f)). We recorded the wind speed and direction at the source using a cup and vane anemometer (Vantage Vue, Davis Instruments, USA) at a data rate of 1 reading per minute (Fig. 5(g)).

In both experiments, the sensor successfully detected enhancements in methane concentration above background levels, demonstrating detection capabilities at very low methane emission flux rates of $< 0.5 \text{ kg h}^{-1}$. Although the methane flow rate was lower, controlled-release B shows much higher enhancement than controlled-release A. This is mainly because the UAV flew much closer to the release point during controlled-release B (< 30 m) compared to controlled-release A (76 to 119 m). Controlled-release B showcases a scenario where leak detection can be performed in very low wind conditions; however, the experimental conditions were not suited to near-field emission rate quantification due to the unsteady plume evolution.

3.3 Emission flux quantification

The flux curtain from controlled-release A was acquired under relatively stable wind conditions and is therefore suitable for flux estimation using the procedure described in Section 2.7. The average ambient temperature during the measurement was $T = 24.2°\text{C} \pm 1°\text{C}$ and the pressure was found to vary with altitude according to the relation $P(z) = -12.1\, z + 100390$ Pa with uncertainty $\Delta P = 75$ Pa. Fig. 6(a) and (b) show heat maps of the measured flux density q for the far and near flux curtains, calculated from the elevated methane concentration, the orthogonal wind field (measured by the anemometer mounted on the UAV), and the density of methane gas, as per Eq. (2).

The corresponding transect-integrated flux densities, $\int_{\text{tr.}} q\, dy$, are shown in Fig. 6(c) and (d), with error bars indicating the propagated 1σ uncertainties. Uncertainty in the measured methane concentration includes 5% for calibration uncertainty and 26 ppb for in-flight measurement resolution (0.1 s averaging time). The background methane concentration, which is averaged over 60 s, has a resolution of 10 ppb. Uncertainty in the wind speed u accounts for the instrument accuracy, $\text{Min}(2\%, 0.1\,\text{ms}^-1)$,

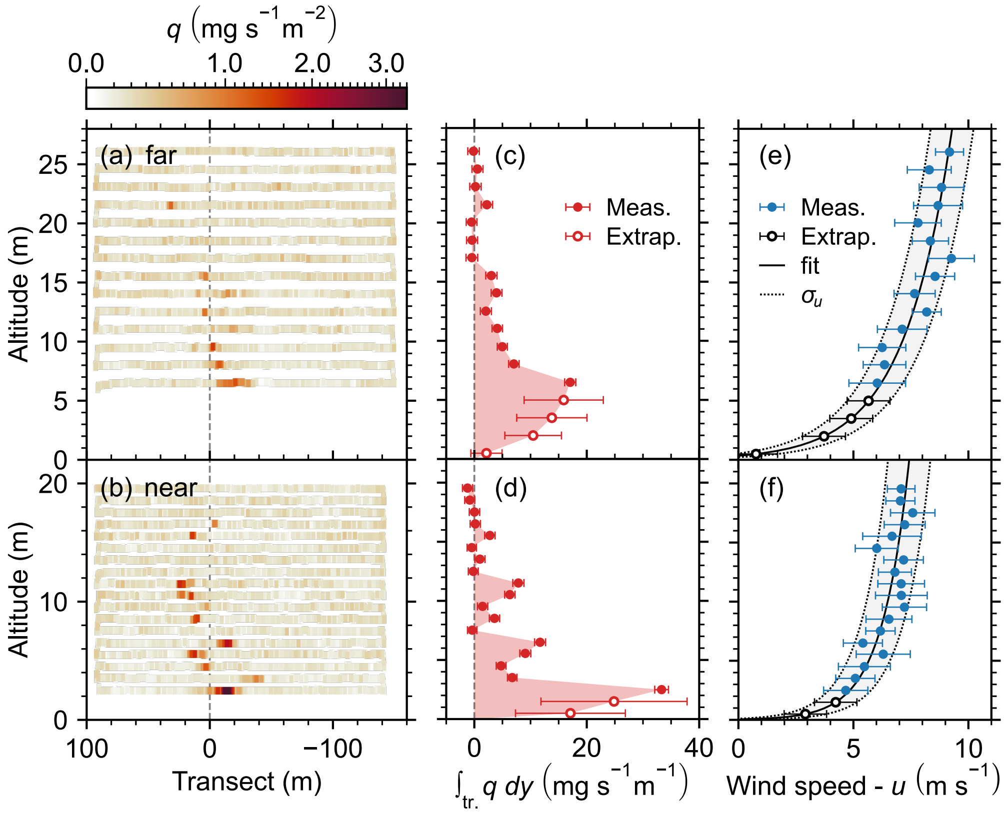

Figure 6. (a, b) Heat maps showing methane flux density along the UAV flight path for CR-A (near and far curtains). (c, d) Corresponding transect-integrated flux density for each horizontal transect. The shaded regions correspond to the estimated total emission flux and error bars indicate 1σ uncertainties. (e, f) Average wind speed and standard deviation along each horizontal transect and fit to logarithmic wind model including $1\sigma_u$ prediction interval. Extrapolated transects are indicated by the open markers.

and the $1\sigma_u$ measurement noise. For the wind direction θ, uncertainty includes 1° for instrument accuracy, 5° for anemometer alignment, and the $1\sigma_\theta$ measurement noise. The lateral position of the DJI Matrice 300 RTK UAV is recorded to a precision of 1 cm.

The open markers indicate 'virtual' transects introduced to extrapolate between the lowest measured transect and the ground, as described in Section 2.7. A constant transect-integrated methane concentration was defined from the lowest transect to the ground, where $\int_{\mathrm{tr.}} [\mathrm{CH_4}]\, dy = 4.3 \pm 1.5\ \mathrm{ppm \cdot m}$ for the far curtain and $9.0 \pm 2.9\ \mathrm{ppm \cdot m}$ for the near curtain. Fitting Eq. 4 to the wind data recorded from the UAV, parameters $u^* = 0.842 \pm 0.024\ \mathrm{ms^{-1}}$ and $z_0 = 0.340 \pm 0.029$ m were obtained for the far flux curtain. For the near curtain, $u^* = 0.475 \pm 0.014\ \mathrm{ms^{-1}}$ and $z_0 = 0.042 \pm 0.005$ m. The differences in the logarithmic wind fields are attributed to the rougher terrain beneath the far flux curtain and to changing wind conditions over time, as the total experiment took 54 minutes, including a 23 minute delay between completing the near curtain and beginning to fly the far curtain.

The shaded regions in Fig. 6(c, d) correspond to the estimates for total methane emission flux, $Q = 0.46 \pm 0.13$ kg h^{-1} and $Q = 0.45 \pm 0.12$ kg h^{-1} for the far and near flux curtains, respectively. The true methane release rate, 0.48 kg h^{-1}, falls within the 2σ uncertainty bounds for both estimated flux rates. The dominant source of error in the estimated flux rate is the extrapolation between the lowest measured transect and the ground. Furthermore, if the lowest measured transect is neglected from the flux calculation and extrapolation is carried out from the next-lowest transect, the computed flux rates would be $Q = 0.27 \pm 0.07$ kg h^{-1} (far) and $Q = 0.26 \pm 0.05$ kg h^{-1} (near), far from the true release rate. This underscores the importance of flying transects as near to the ground as possible. The impact of the linear interpolations used when integrating over the flux curtain is not considered here, and should be the subject of further study.

During experiment CR-B, the wind was very low, with 53% of recorded speeds < 0.5 m s^{-1} (see Fig. 5(f)). Furthermore, the measurements were performed very close to the methane source. As such, the methane plume was unstable and the acquired flux box was not suitable for emission flux estimation.

4 Conclusions

UAV-based gas measurements can cover spatio-temporal measurement gaps between ground-based measurements and crewed aircraft measurements, offering exceptional versatility. In particular, small UAVs are easier to transport and are typically associated with less restrictive regulations than large UAVs ($>$ 25 kg), underscoring the importance of developing compatible lightweight gas sensing platforms. In this work, we developed an ultra-lightweight and compact methane sensor platform for in-situ measurements and deployed it on a small enterprise-grade UAV in controlled-release experiments to evaluate its potential to quantify fugitive methane emissions.

The sensor is based on tunable diode laser absorption spectroscopy and employs an open-path multi-pass absorption cell for fast (100 Hz) response times and wavelength modulation spectroscopy for improved signal-to-noise. A small single board computer and custom data acquisition PCB has facilitated the miniaturization of a complete data acquisition and control system with real-time onboard WMS data processing and local data storage capabilities. The sensor achieves an in-flight resolution of 6.5 ppb at 1 Hz. The sensor weighs just 1.2 kg and consumes approximately 11 W of electrical power when the ambient temperature is around 20°C, enabling uninterrupted flight missions exceeding 2 hours.

The system detected emissions for release rates of 0.2 and 0.48 kg h^{-1}. Using a direct mass balance flux quantification approach, the 0.48 kg h^{-1} emission rate was obtained to within 6.25% under steady winds and at downwind distances of 76 and 119 m from the release point. The accuracy of the retrieved emission rate depends on the ability to fly close to the ground, emphasizing the benefits of near-ground measurements offered by small UAV platforms and compatible gas sensors. To fully evaluate this UAV-based emission rate quantification approach, further systematic and statistical studies are needed to assess how variables such as meteorological conditions, source parameters, flight patterns, and terrain topography influence the probability of detection and quantification accuracy.

The ultra-lightweight gas analyzer presented here targets methane gas in the mid-IR using a HgCdTe photodetector and a GaSb-based DFB laser centered at 3270.4 nm. Where possible, commercially available off-the-shelf components were used in the sensor design to facilitate the adoption and widespread use of this measurement technique. A lower-cost system could be achieved using silver or aluminum mirrors in place of gold and replacing the mid-IR light source and photodetector with near-IR alternatives for applications where the enhanced resolution provided by mid-IR sources is not required.

The core design also remains readily adaptable. Beyond methane, the sensor design and measurement methodology can be adapted to other gaseous species by substituting the light source and photodetector and making certain configuration changes based on the characteristics of the target gas species and the environment.

Overall, we have developed a high-precision ultra-lightweight gas sensor optimized for deployment on small UAVs. We have demonstrated that this is a promising method for targeted detection and quantification of emission sources, including very small ones, near the ground and over terrain that is inaccessible to or cannot be measured by alternative measurement platforms.

Code and data availability. The data and code used in this paper are available from the corresponding author upon request.

Author contributions. **Meghan N. Beattie**: methodology, investigation, data curation, formal analysis, visualization, software, writing – original draft. **Chase Sun**: methodology, validation, software. **Roger MacLeod**: methodology, investigation, date curation, writing - review & editing. **Nicaulas Sabourin**: methodology, writing - review & editing. **Peter D. Morse**: funding acquisition, resources, writing - review & editing. **Greg. J. Smallwood**: conceptualization, funding acquisition, supervision, writing - review & editing. **Joel C. Corbin**: supervision, resources, writing - review & editing. **Jalal Norooz Oliaee**: conceptualization, methodology, validation, investigation, funding acquisition, project administration, writing – original draft.

Competing interests. The authors declare that they have no conflict of interest.

Acknowledgements. The authors would like to thank Eric Bachalo for assistance in programming the single board computer; Ross Cheriton, Mhanna Mhanna, and Mohammad Salehi for assistance in carrying out the field work; and Haydn Sims and Simon-Alexandre Lussier for conducting the calibration and Allan-Werle measurements.

Financial support. This work was supported by the government of Canada. MNB was supported by a grant from Natural Resources Canada's Office of Energy Research and Development (NRC-23-137).

References

Berchet, A., Pison, I., Crill, P. M., Thornton, B., Bousquet, P., Thonat, T., Hocking, T., Thanwerdas, J., Paris, J. D., and Saunois, M.: Using ship-borne observations of methane isotopic ratio in the Arctic Ocean to understand methane sources in the Arctic, Atmospheric Chemistry and Physics, 20, 3987–3998, https://doi.org/10.5194/acp-20-3987-2020, 2020.

Blackmore, D. C., Hickey, J.-P., Wigle, A., Osadetz, K., and Daun, K. J.: A Bayesian technique for quantifying methane emissions using vehicle-mounted sensors with a Gaussian plume model, Atmospheric Environment, p. 121002, https://doi.org/10.1016/j.atmosenv.2024.121002, 2024.

Bolek, A., Heimann, M., and Göckede, M.: UAV-based in situ measurements of CO2 and CH4 fluxes over complex natural ecosystems, Atmospheric Measurement Techniques, 17, 5619–5636, https://doi.org/10.5194/amt-17-5619-2024, 2024.

Bonne, J. L., Donnat, L., Albora, G., Burgalat, J., Chauvin, N., Combaz, D., Cousin, J., Decarpenterie, T., Duclaux, O., Dumelié, N., Galas, N., Juery, C., Parent, F., Pineau, F., Maunoury, A., Ventre, O., Bénassy, M. F., and Joly, L.: A measurement system for CO2and CH4emissions quantification of industrial sites using a new in situ concentration sensor operated on board uncrewed aircraft vehicles, Atmospheric Measurement Techniques, 17, 4471–4491, https://doi.org/10.5194/amt-17-4471-2024, 2024.

Caulton, D. R., Li, Q., Bou-Zeid, E., Fitts, J. P., Golston, L. M., Pan, D., Lu, J., Lane, H. M., Buchholz, B., Guo, X., McSpiritt, J., Wendt, L., and Zondlo, M. A.: Quantifying uncertainties from mobile-laboratory-derived emissions of well pads using inverse Gaussian methods, Atmospheric Chemistry and Physics, 18, 15 145–15 168, https://doi.org/10.5194/acp-18-15145-2018, 2018.

Cossel, K. C., Waxman, E. M., Giorgetta, F. R., Cermak, M., Coddington, I. R., Hesselius, D., Ruben, S., Swann, W. C., Truong, G.-W., Rieker, G. B., and Newbury, N. R.: Open-path dual-comb spectroscopy to an airborne retroreflector, Optica, 4, 724, https://doi.org/10.1364/optica.4.000724, 2017.

Cui, R., Dong, L., Wu, H., Li, S., Yin, X., Zhang, L., Ma, W., Yin, W., and Tittel, F. K.: Calculation model of dense spot pattern multi-pass cells based on a spherical mirror aberration, Optics Letters, 44, 1108, https://doi.org/10.1364/ol.44.001108, 2019.

Detto, M., Verfaillie, J., Anderson, F., Xu, L., and Baldocchi, D.: Comparing laser-based open- and closed-path gas analyzers to measure methane fluxes using the eddy covariance method, Agricultural and Forest Meteorology, 151, 1312–1324, https://doi.org/10.1016/j.agrformet.2011.05.014, 2011.

Dooley, J. F., Minschwaner, K., Dubey, M. K., Abbadi, S. H. E., Sherwin, E. D., Meyer, A. G., Follansbee, E., and Lee, J. E.: A new aerial approach for quantifying and attributing methane emissions: Implementation and validation, Atmospheric Measurement Techniques, 17, 5091–5111, https://doi.org/10.5194/amt-17-5091-2024, 2024.

Engel, G. S. and Moyer, E. J.: Precise multipass Herriott cell design: Derivation of controlling design equations, Optics Letters, 32, 704, https://doi.org/10.1364/OL.32.000704, 2007.

Fish, R., Municchi, F., Sprinkle, B., and Hammerling, D.: A comparison of turbulent CFD with Gaussian dispersion models on a methane emission test site, Atmospheric Environment: X, 27, https://doi.org/10.1016/j.aeaoa.2025.100326, 2025.

Golston, L. M., Tao, L., Brosy, C., Schäfer, K., Wolf, B., McSpiritt, J., Buchholz, B., Caulton, D. R., Pan, D., Zondlo, M. A., Yoel, D., Kunstmann, H., and McGregor, M.: Lightweight mid-infrared methane sensor for unmanned aerial systems, Applied Physics B: Lasers and Optics, 123, https://doi.org/10.1007/s00340-017-6735-6, 2017.

Gordon, M., Li, S. M., Staebler, R., Darlington, A., Hayden, K., O'Brien, J., and Wolde, M.: Determining air pollutant emission rates based on mass balance using airborne measurement data over the Alberta oil sands operations, Atmospheric Measurement Techniques, 8, 3745–3765, https://doi.org/10.5194/amt-8-3745-2015, 2015.

Han, T., Liggio, J., Narayan, J., Liu, Y., Hayden, K., Mittermeier, R., Darlington, A., Wheeler, M., Cober, S., Zhang, Y., Xie, C., Yang, Y., Huang, Y., Wolde, M., Smyth, S., Barrigar, O., and Li, S. M.: Quantification of Methane Emissions from Cold Heavy Oil Production with Sand Extraction in Alberta and Saskatchewan, Canada, Environmental Science and Technology, https://doi.org/10.1021/acs.est.4c02333, 2024.

Khaleghi, A., MacKay, K., Darlington, A., James, L. A., and Risk, D.: Methane emission rate estimates of offshore oil platforms in Newfoundland and Labrador, Canada, Elementa, 12, https://doi.org/10.1525/elementa.2024.00025, 2024.

Kumar, P., Broquet, G., Yver-Kwok, C., Laurent, O., Gichuki, S., Caldow, C., Cropley, F., Lauvaux, T., Ramonet, M., Berthe, G., Martin, F., Duclaux, O., Juery, C., Bouchet, C., and Ciais, P.: Mobile atmospheric measurements and local-scale inverse estimation of the location and rates of brief CH4 and CO2 releases from point sources, Atmospheric Measurement Techniques, 14, 5987–6003, https://doi.org/10.5194/amt-14-5987-2021, 2021.

Kumar, P., Broquet, G., Caldow, C., Laurent, O., Gichuki, S., Cropley, F., Yver-Kwok, C., Fontanier, B., Lauvaux, T., Ramonet, M., Shah, A., Berthe, G., Martin, F., Duclaux, O., Juery, C., Bouchet, C., Pitt, J., and Ciais, P.: Near-field atmospheric inversions for the localization and quantification of controlled methane releases using stationary and mobile measurements, Quarterly Journal of the Royal Meteorological Society, 148, 1886–1912, https://doi.org/10.1002/qj.4283, 2022.

Maazallahi, H., Delre, A., Scheutz, C., Fredenslund, A. M., Schwietzke, S., Gon, H. D. V. D., and Röckmann, T.: Intercomparison of detection and quantification methods for methane emissions from the natural gas distribution network in Hamburg, Germany, Atmospheric Measurement Techniques, 16, 5051–5073, https://doi.org/10.5194/amt-16-5051-2023, 2023.

MacKay, K., Lavoie, M., Bourlon, E., Atherton, E., O'Connell, E., Baillie, J., Fougère, C., and Risk, D.: Methane emissions from upstream oil and gas production in Canada are underestimated, Scientific Reports, 11, https://doi.org/10.1038/s41598-021-87610-3, 2021.

McDermitt, D., Burba, G., Xu, L., Anderson, T., Komissarov, A., Riensche, B., Schedlbauer, J., Starr, G., Zona, D., Oechel, W., Oberbauer, S., and Hastings, S.: A new low-power, open-path instrument for measuring methane flux by eddy covariance, in: Applied Physics B: Lasers and Optics, vol. 102, pp. 391–405, ISSN 09462171, https://doi.org/10.1007/s00340-010-4307-0, 2011.

Norooz Oliaee, J., Sabourin, N. A., Festa-Bianchet, S. A., Gupta, J. A., Johnson, M. R., Thomson, K. A., Smallwood, G. J., and Lobo, P.: Development of a Sub-ppb Resolution Methane Sensor Using a GaSb-Based DFB Diode Laser near 3270 nm for Fugitive Emission Measurement, ACS Sensors, 7, 564–572, https://doi.org/10.1021/acssensors.1c02444, 2022.

Scheutz, C., Knudsen, J. E., Vechi, N. T., and Knudsen, J.: Validation and demonstration of a drone-based method for quantifying fugitive methane emissions, Journal of Environmental Management, 373, https://doi.org/10.1016/j.jenvman.2024.123467, 2025.

Shaw, J. T., Shah, A., Yong, H., and Allen, G.: Methods for quantifying methane emissions using unmanned aerial vehicles: A review, https://doi.org/10.1098/rsta.2020.0450, 2021.

Takriti, M., Wynn, P. M., Elias, D. M., Ward, S. E., Oakley, S., and McNamara, N. P.: Mobile methane measurements: Effects of instrument specifications on data interpretation, reproducibility, and isotopic precision, Atmospheric Environment, 246, https://doi.org/10.1016/j.atmosenv.2020.118067, 2021.

Thorpe, M. J., Kreitinger, A., Seger, E., Greenfield, N., Wilson, C., Trey, P., Kreitinger, S., Gordon, S., Schmitt, R., and Roos, P.: Gas Mapping LiDAR for large-area leak detection and emissions monitoring applications, in: Conference on Lasers and Electro-Optics, p. AF2B.1, Optica Publishing Group, https://doi.org/10.1364/CLEO_AT.2017.AF2B.1, 2017.

Tuzson, B., Graf, M., Ravelid, J., Scheidegger, P., Kupferschmid, A., Looser, H., Morales, R. P., and Emmenegger, L.: A compact QCL spectrometer for mobile, high-precision methane sensing aboard drones, Atmospheric Measurement Techniques, 13, 4715–4726, https://doi.org/10.5194/amt-13-4715-2020, 2020.

Tyner, D. R. and Johnson, M. R.: Where the Methane Is - Insights from Novel Airborne LiDAR Measurements Combined with Ground Survey Data, Environmental Science and Technology, 55, 9773–9783, https://doi.org/10.1021/acs.est.1c01572, 2021.

Visscher, A. D.: Air Dispersion Modeling, John Wiley & Sons, Inc., 2014.

Vogel, F., Ars, S., Wunch, D., Lavoie, J., Gillespie, L., Maazallahi, H., Röckmann, T., Nęcki, J., Bartyzel, J., Jagoda, P., Lowry, D., France, J., Fernandez, J., Bakkaloglu, S., Fisher, R., Lanoiselle, M., Chen, H., Oudshoorn, M., Yver-Kwok, C., Defratyka, S., Morgui, J. A., Estruch, C., Curcoll, R., Grossi, C., Chen, J., Dietrich, F., Forstmaier, A., van der Gon, H. A. D., Dellaert, S. N., Salo, J., Corbu, M., Iancu, S. S., Tudor, A. S., Scarlat, A. I., and Calcan, A.: Ground-Based Mobile Measurements to Track Urban Methane Emissions from Natural Gas in 12 Cities across Eight Countries, Environmental Science and Technology, 58, 2271–2281, https://doi.org/10.1021/acs.est.3c03160, 2024.

Werle, P.: Accuracy and precision of laser spectrometers for trace gas sensing in the presence of optical fringes and atmospheric turbulence, in: Applied Physics B: Lasers and Optics, vol. 102, pp. 313–329, ISSN 09462171, https://doi.org/10.1007/s00340-010-4165-9, 2011.

Wharton, S., Brown, M. J., Dexheimer, D., Fast, J. D., Newsom, R. K., Schalk, W. W., and Wiersema, D. J.: Capturing plume behavior in complex terrain: an overview of the Nevada National Security Site Meteorological Experiment (METEX21), Frontiers in Earth Science, 11, https://doi.org/10.3389/feart.2023.1251153, 2023.

Zhou, X., Montazeri, A., and Albertson, J. D.: Mobile sensing of point-source gas emissions using Bayesian inference: An empirical examination of the likelihood function, Atmospheric Environment, 218, https://doi.org/10.1016/j.atmosenv.2019.116981, 2019.